



Adaptive lensless microscopic imaging with unknown phase modulation

XIANGYU CHEN,¹ HAO SHA,¹ CHUNYU CHEN,² YUAN JIANG,¹
WENZHEN ZOU,¹ AND YONGBING ZHANG^{1,*}

¹School of Computer Science and Technology, Harbin Institute of Technology, Shenzhen, Guangdong 518055, China

²School of Computer Science and Technology, Harbin Institute of Technology, Harbin 150001, China

*ybhang08@hit.edu.cn

Abstract: Lensless imaging is a popular research field because of its small size, wide field-of-view, and low aberration in recent years. However, some traditional lensless imaging methods suffer from slow convergence, mechanical errors, and conjugate solution interference, which limit their further application and development. In this work, we proposed a lensless imaging method based on a spatial light modulator (SLM) with unknown phase modulation values. In our imaging system, the SLM is utilized to modulate the wavefront of the object. When the phase modulation values of the SLM are inaccurate or unknown, conventional algorithms such as amplitude-phase retrieval (APR) or the extended ptychographic iterative engine (ePIE) fail to reconstruct the complex amplitude information of the object. To address this challenge, we introduce a novel approach that combines ptychographic scanning along a spiral path with the ePIE algorithm, enabling accurate reconstruction of the original image. We further analyze the effect of modulation function and the characteristics of the coherent light source on the quality of the reconstructed image. The experiments show that the proposed method is superior to traditional methods in terms of recovering speed and accuracy, with the recovering resolution up to 14 μm in the reconstruction of the USAF phase plate image.

© 2025 Optica Publishing Group under the terms of the [Optica Open Access Publishing Agreement](#)

1. Introduction

Lensless imaging systems can recover the optical field distribution of objects from mixed signals without requiring any optical lenses [1], thereby simplifying the illumination and imaging pathways. Owing to the advantages of miniaturization, lensless imaging systems exhibit a wide range of applications across various scientific and technological domains [2–5]. In terms of microscopic imaging, conventional microscope system is unable to achieve both high resolution and wide field-of-view (FOV), and the spatial bandwidth product (SBP) is limited by the FOV, while lensless cameras can theoretically reach the diffraction limit resolution with the advantages of both high SBP and low aberration [6,7].

In incoherent imaging system, the light intensity satisfies a linear relationship, so the image captured by sensor is the result of convolution of the object with the point spread function (PSF) of the system. The PSF can be calibrated by modulating the wavefront of the object with an encoding element (also known as mask) [8–13]. Although incoherent lensless modulation imaging is able to reconstruct the final image using deconvolution algorithms, mask-based reconstruction algorithm still suffers from insufficient luminous flux, poor frequency domain characteristics and slow convergence speed. In recent years, various deconvolution networks based on deep learning have been proposed [14–18], effectively improving reconstruction quality and accelerating convergence. However, incoherent imaging cannot recover the phase information of the object, limiting its further applications.

Different from incoherent imaging, the complex amplitude is linear during the propagation of coherent light, making it possible to recover the phase information. In recent years, coded ptychographic imaging has become a prominent approach in lensless coherent imaging. Conventional ptychography relies on a localized illumination probe and employs lateral scanning of the sample to acquire a series of diffraction patterns, which are subsequently processed using iterative phase retrieval algorithms to reconstruct the complex amplitude distribution of the specimen. However, these methods rely on the movement of light sources or sensors, which will inevitably introduce the mechanical errors. Phase recovery can be divided into interference-based methods [19–21] and intensity-based methods [22,23]. The main application of the interference-based method is holographic imaging, where the principle is to convert phase information into observable intensity information by introducing a reference light that interferes with the light carrying object information [24–26]. Although the holographic imaging method requires a relatively low amount of data, the experiment is difficult to carry out due to the high requirements for the stability of the optical path. Moreover, the requirement to acquire multiple diverse images renders these methods unsuitable for imaging dynamic samples. Therefore, Y. Gao *et al.* implemented a high-frame-rate coded ptychography based on diffuser modulation, where a random scattering element is used to modulate the sample's wavefront, thereby replacing the need for mechanical scanning. And they proposed a general computational framework, termed spatiotemporally regularized inversion (STRIVER), to achieve motion-resolved, reference-free holographic imaging with high fidelity [27]. The intensity-based method applies phase recovery such as Gerchberg-Saxton (GS) algorithm or its variants for image reconstruction [28–30]. However, the GS algorithm requires objects to satisfy the sparsity condition and has relatively slow convergence. In contrast, ptychographic iterative engine (PIE) algorithm solves the complex amplitude distribution of high-resolution samples by acquiring a series of low-resolution images [31]. G. Zheng *et al.* placed the diffuser on the sensor surface and moved it through a two-dimensional high-precision displacement platform to modulate the object wavefront, enabling high-resolution pathology imaging with a wide field-of-view [32]. C. Lu *et al.* replaced mechanical scanning devices with LED arrays, to reduce the impact of mechanical errors [33]. B. Wang *et al.* proposed a coherent modulation imaging (CMI) algorithm based on unknown modulation, which enables the simultaneous reconstruction of the sample and the retrieval of the unknown modulator function. By performing multiple measurements with the same modulator, applying an averaging operation to refine the estimated modulation function, and imposing amplitude constraints on the modulator, this approach enhances the independence and flexibility of CMI [34]. S. Jiang *et al.* proposed a parallel coded ptychography approach that utilizes a lensless scattering surface for phase encoding and employs a high numerical aperture (NA) detection scheme to enhance imaging resolution [35]. Subsequently, they provided a comprehensive introduction to the applications of spatial-domain coded ptychography (CP) and Fourier-domain ptychography (FP) in visible light imaging, detailing the experimental implementation procedures and analyzing the advantages and limitations of different ptychographic imaging strategies [36]. L. Liu *et al.* proposed a simple-to-implement and noise-robust maximum-likelihood HDR (ML-HDR) image fusion approach to broaden the effective numerical aperture (NA) of ptychographic imaging [37]. G. Weinberg *et al.* have introduced a simple lensless micro-endoscopic approach for coherent reflection imaging, utilizing readily available multi-core fibers [38]. P. Song *et al.* integrated the principles of synthetic aperture radar (SAR) imaging and ptychography to achieve super-resolution micro-endoscopic imaging by hand-holding a lensless fiber bundle tip. This technique not only simplifies the experimental setup but also enhances the adaptability of the system, offering new possibilities for future medical and industrial applications [39].

Another method of wavefront modulation is to use a spatial light modulator (SLM). The SLM executes phase modulation by employing a modulation pattern, typically represented as a grayscale image, and translating the grayscale values into corresponding phase shifts as

defined by its modulation curve. M. Deweert *et al.* used SLM as a programmable amplitude mask to achieve incoherent imaging in natural light [40]. Y. Wu *et al.* achieved lensless high-resolution microscopic dynamic imaging of multiple samples and multiple scenes using high performance SLM [41]. The reconstruction performance of these methods depends on the accuracy of the modulation curve, which imposes a high demand on the SLM hardware. In practical applications, deviations between the phase-grayscale modulation curve of the SLM and the ideal linear relationship arise due to manufacturing errors and cost constraints. Consequently, the applied phase modulation on the SLM may deviate from the expected ideal values. In such cases, a calibration curve must be employed in the algorithm to correct the phase modulation values. When the calibration curve is unknown or contains calibration errors, both traditional Amplitude-Phase Retrieval (APR) algorithms [42] and the expended ptychographic iterative engine (ePIE) algorithm [43] with random scanning paths struggle to accurately reconstruct the complex amplitude of the sample.

To address these problems, we report a lensless imaging method based on SLM and ptychographic algorithm. Specifically, leveraging the principles of tomography, we incorporate the concept of ptychographic scanning into wavefront sensing by employing modulation patterns with overlapping regions. Combining with the ePIE algorithm, our method can recover the amplitude and phase information simultaneously, which improves the robustness and convergence speed of the system. In the field of coded ptychography, compared to high-resolution coded ptychography methods [35,36,44], our approach replaces mechanical scanning with spatial light modulator (SLM) modulation, endowing the system with enhanced flexibility and adaptability. Conventional mechanical scanning systems are susceptible to positioning errors and mechanical vibrations, whereas the SLM-based scheme ensures superior system stability. The SLM enables millisecond-level switching between different modulation patterns, significantly outperforming mechanical scanning systems that require prolonged motion time. This advantage makes our method particularly promising for dynamic imaging applications. Furthermore, eliminating mechanical scanning components results in a more compact hardware configuration, reduces experimental complexity, and enhances compatibility with portable imaging devices. The contributions of our work mainly include: Despite errors in the phase modulation values of the SLM, the complex amplitude information of the object can still be successfully recovered. The mechanical displacement platform is replaced with a programmable random pattern, and the amplitude and phase of the object are reconstructed utilizing a ptychographic scanning algorithm. A real coherent lensless imaging system is built, and the effects of modulation patterns, algorithmic parameters, and the light source on the quality of the reconstructed images are systematically evaluated.

2. Methods

The schematic diagram of proposed lensless imaging system is shown in Fig. 1(a). In this system, we utilize a laser as coherent light source and convert it to parallel light by a collimator. Inspired by [45], we also insert two polarizers in the front and rear of the sample to fix the wavelength and polarization state of the light source to obtain stable modulation. Sample's optical field diffracts from the object plane to SLM plane after propagating d_1 distance. The SLM changes the complex amplitude state of the unit by controlling the directions of liquid crystal molecules through voltage, thus realizing the modulation. Finally, the modulated complex amplitude is propagated d_2 distance to the sensor plane. Since there is no lens in the imaging system, the object cannot be discerned from the image captured by CCD.

A series of coherent diffraction images can be acquired by changing the modulation mode of the SLM. For the system shown in Fig. 1(a), the intensity image produced by n -th modulated

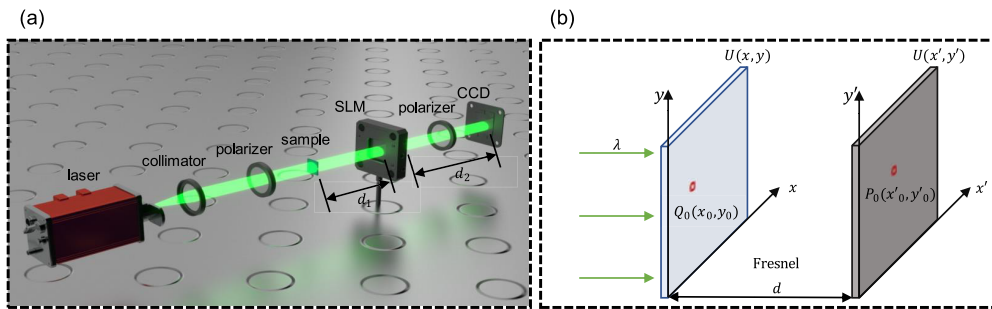


Fig. 1. The schematic diagram of proposed lensless imaging system. (a) The optical path of our system and (b) The Fresnel diffraction process.

pattern on CCD can be summarized as:

$$I_n(\mathbf{r}_{\text{ccd}}) = |prop_{d2}(SLM_n * prop_{d1}(O(\mathbf{r}_{\text{sample}})))|^2, \quad (1)$$

where $I_n(\mathbf{r}_{\text{ccd}})$ is the n -th intensity measurement on CCD, $O(\mathbf{r}_{\text{sample}})$ is the complex amplitude distribution of the object, \mathbf{r} denotes the coordinates on the corresponding plane, SLM_n is the modulation function, also named pattern, corresponding to the n -th measurement, $prop_d$ represents the diffraction process with propagation distance d . d_1 is the distance between object and SLM, and d_2 is the distance between SLM and CCD. As shown in Fig. 1(b), when the diffraction distance is relatively small, the diffraction process can be approximated as Fresnel diffraction, and $prop_d$ has the following expression:

$$prop_d(O(x, y)) = \frac{e^{jkd}}{j\lambda d} \iint_{-\infty}^{\infty} O(x, y) \exp \left\{ j \frac{k}{2d} [(x - x')^2 + (y - y')^2] \right\} dx dy, \quad (2)$$

where the $O(\cdot)$ is the complex amplitude distribution of the plane, (x, y) and (x', y') represent the coordinates of different diffraction planes respectively, $k = 2\pi/\lambda$ is the wave vector, λ is the wave length, and d is the distance between the two diffraction planes. Further, we define an intermediate variable:

$$h(x, y) = \frac{e^{jkd}}{j\lambda d} \exp \left\{ j \frac{k}{2d} (x^2 + y^2) \right\}, \quad (3)$$

then the Fresnel diffraction process $prop_d(O(x, y))$ can be expressed as :

$$prop_d(O(x, y)) = O(x, y) \otimes h(x, y), \quad (4)$$

where " \otimes " denotes convolution. Similarly, the image of the SLM plane can be calculated from the sensor plane according to the Fresnel inverse diffraction formula:

$$prop_{-d}(O(x', y')) = \frac{e^{jkd}}{j\lambda d} \iint_{-\infty}^{\infty} O(x', y') \exp \left\{ -j \frac{k}{2d} [(x - x')^2 + (y - y')^2] \right\} dx dy. \quad (5)$$

Ideally, it is assumed that the phase modulation values of the SLM maintain a linear relationship with the grayscale values of the pattern applied to it. However, because of the influence of hardware parameters within the SLM, the modulation curve is inherently nonlinear. Generally, it is necessary to obtain a calibrated modulation curve of the SLM, which can be used to correct errors in the phase modulation values. To demonstrate the impact of uncorrected phase modulation errors, experiments were conducted using a USAF resolution target. The SLM with a phase-grayscale calibration modulation curve (the red curve in Fig. 2(a)) was used to load modulation patterns in

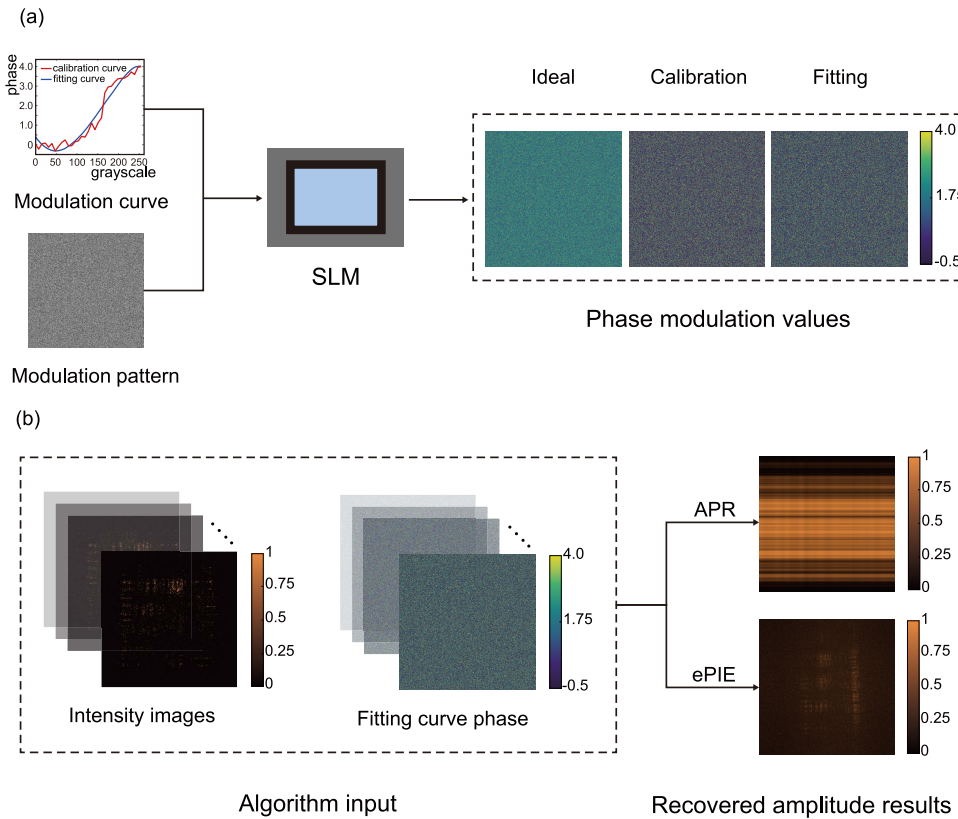


Fig. 2. Lensless imaging reconstruction results based on the APR algorithm and the ePIE algorithm in the presence of deviations in the modulation curve. (a) The phase modulation values corresponding to the modulation patterns under different modulation curves. Substantial discrepancies are observed between the phase modulation values predicted by the ideal linear relationship or the fitted curve and those derived from the calibration curve. (b) Algorithm inputs and recovered amplitude results of the APR and the ePIE algorithm. When the phase values corresponding to the fitting curve are used as inputs to the algorithm, both the APR algorithm and the ePIE algorithm fail to produce accurate reconstruction results.

the experiments, and the corresponding intensity images were captured. During reconstruction, modulation values corresponding to the fitting curve (the blue curve in Fig. 2(a)) were utilized as inputs to the algorithm. The experiment results are shown in Fig. 2(b). Without correcting the errors in phase modulation, the complex amplitude information cannot be reconstructed by either APR or ePIE algorithm. This indicates that in systems utilizing different SLMs, the correction process needs to be reiterated. To enhance the universality of our method and enable it to recover the object's complex amplitude information even when the SLM modulation curve is unknown, we have redesigned the loading method of phase modulation patterns on the SLM, as shown in Fig. 3. We introduced the concept of ptychographic scanning with a spiral scan path, which has been discussed in previous works [46]. Specifically, we use a randomly uniformly distributed image with a size of 768×768 as the initial central phase modulation pattern and generate a sequence of 169 grayscale images based on a spiral scan with 2 pixel offset, as shown in Fig. 3(a) and Fig. 3(b). This pixel offset was chosen to maintain a sufficient overlap ratio, ensuring stable ptychographic reconstruction while balancing computational efficiency. We load these patterns

onto the SLM in a predefined sequence for ptychographic scanning and employ the ePIE algorithm to recover the complex amplitude of the object. The spiral scanning path enables a smooth spatial shift of the modulation pattern, ensuring a more uniform distribution of SLM modulation errors and reducing the impact of localized errors on imaging results. Compared to traditional fixed-grid scanning, the spiral scanning approach mitigates the accumulation of local errors by effectively averaging them over multiple measurements, thereby enhancing the robustness of the reconstruction algorithm. Furthermore, the introduction of smooth and continuous spatial displacements provides more stable phase information redundancy, improving the convergence rate and accuracy of the ePIE algorithm when handling nonlinear phase modulation errors, which can greatly reduce the impact of SLM modulation errors. The intensity images captured by CCD are shown in Fig. 3(c) and also available in the [Visualization 1](#).

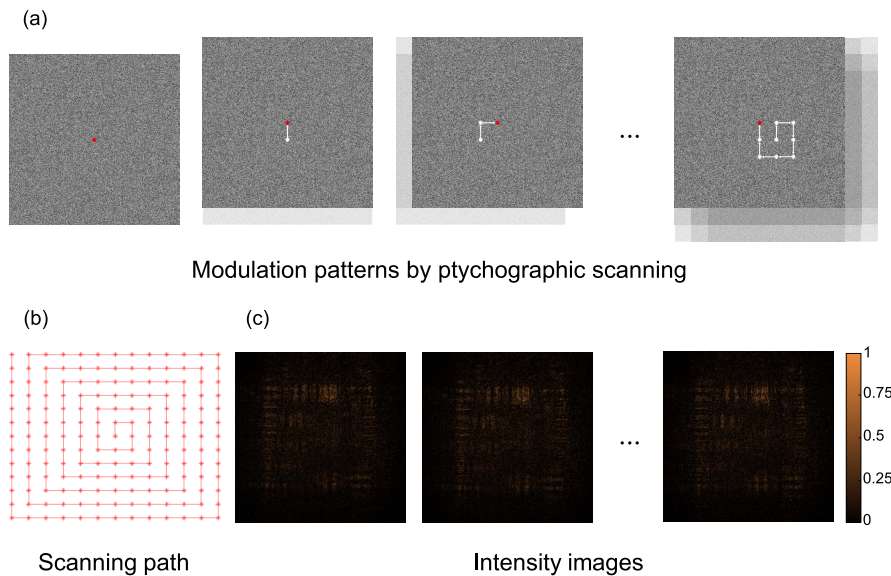


Fig. 3. The modulation process of SLM. (a) A series of modulation patterns of the SLM, each of which has a fixed offset relationship between patterns. (b) The spiral scanning sequence of the patterns. (c) A series of diffraction intensity images of USAF resolution target captured by digital sensor under different patterns.

The initial purpose of the ePIE algorithm was to correct errors in the illumination function by simultaneously updating the illumination function while updating the object's complex amplitude function. This is crucial in experiments using multi-angle illumination. In the system constructed in this paper, the light source remains unchanged, and the variation occurs in the phase modulation pattern. Therefore, the ePIE algorithm updates the diffraction complex amplitude of the object on the SLM plane while also updating the pattern. The wavefront of the recovered object in the SLM plane and the initial uniform random pattern of the SLM for the first measurement are $O_0^{SLM}(\mathbf{r}_{SLM})$ and $P_0(\mathbf{r}_{SLM})$, respectively. Since there are only translational relations between different modulation patterns, the pattern of the n -th measurement can be expressed as $P_n(\mathbf{r}_{SLM} - \mathbf{s}_n)$, where \mathbf{s}_n denotes the pixel displacement between different patterns. The modulated complex amplitude $\Psi(\mathbf{r}_{SLM})$ is then propagated to the CCD plane by the Fresnel diffraction formula, and replaces its amplitude with the square root of the real image captured by the digital sensor, $\sqrt{I_n(\mathbf{r}_{CCD})}$. The complex amplitudes after replacement in the CCD plane is further back propagated to the SLM plane, denoted by $\Psi'(\mathbf{r}_{SLM})$, according to the Fresnel inverse

diffraction formula. The inputs of next iteration, $O_{n+1}^{SLM}(\mathbf{r}_{SLM})$ and $P_{n+1}(\mathbf{r}_{SLM})$, can be updated as:

$$O_{n+1}^{SLM}(\mathbf{r}_{SLM}) = O_n^{SLM}(\mathbf{r}_{SLM}) + \alpha \frac{\bar{P}_n(\mathbf{r}_{SLM} - \mathbf{s}_n)}{|P_n(\mathbf{r}_{SLM} - \mathbf{s}_n)|_{\max}^2} \times (\Psi'_n(\mathbf{r}_{SLM}) - \Psi_n(\mathbf{r}_{SLM})), \quad (6)$$

$$P_{n+1}(\mathbf{r}_{SLM} - \mathbf{s}_n) = P_n(\mathbf{r}_{SLM} - \mathbf{s}_n) + \beta \frac{\bar{O}_n^{SLM}(\mathbf{r}_{SLM})}{|O_n^{SLM}(\mathbf{r}_{SLM})|_{\max}^2} \times (\Psi'_n(\mathbf{r}_{SLM}) - \Psi_n(\mathbf{r}_{SLM})), \quad (7)$$

where α and β are the iterative update coefficients, usually taken as 1, and \bar{P}_n and \bar{O}_n^{SLM} denote the conjugate of the corresponding values respectively. The $P_{n+1}(\mathbf{r}_{SLM} - \mathbf{s}_n)$ also needs to be re-shifted by \mathbf{s}_n pixels to get the initial pattern, $P_{n+1}(\mathbf{r}_{SLM})$. To clearly demonstrate the ePIE-based lensless reconstruction algorithm, the pseudocode is given as Algorithm 1. We conducted simulation experiments to quantitatively analyze the reconstruction results of the algorithm when errors are present in the SLM modulation curve, detailed in the [Supplement 1](#) Fig.S2.

Algorithm 1. ePIE-based lensless reconstruction algorithm

Input: Diffraction images $I_n(n = 1, 2, \dots, N)$ with the translational shift of the pattern
Output: Complex amplitude of the object $O(\mathbf{r}_{sample})$ and the modulation function of SLM $P(\mathbf{r}_{SLM})$

- 1: Initialize the complex amplitude on SLM plane $O_0^{SLM}(\mathbf{r}_{SLM})$ and $P_0(\mathbf{r}_{SLM})$, and specify the number of iterations M
- 2: **for** $m=1:M$ **do**
- 3: **for** $n=1:N$ **do**
- 4: $\Psi_n(\mathbf{r}_{SLM}) = O_n^{SLM}(\mathbf{r}_{SLM}) * P_n(\mathbf{r}_{SLM} - \mathbf{s}_n)$
- 5: $\Phi_n(\mathbf{r}_{ccd}) = prop_{d2}(\Psi_n(\mathbf{r}_{SLM}))$
- 6: $\Phi'_n(\mathbf{r}_{ccd}) = \sqrt{I_n(\mathbf{r}_{ccd})} \exp(j \cdot \angle \Phi_n(\mathbf{r}_{ccd}))$
- 7: $\Psi'_n(\mathbf{r}_{SLM}) = prop_{-d2}(\Phi'_n(\mathbf{r}_{ccd}))$
- 8: Update the $O_{n+1}^{SLM}(\mathbf{r}_{SLM})$ using Eq. (6)
- 9: Update the $P_{n+1}(\mathbf{r}_{SLM} - \mathbf{s}_n)$ using Eq. (7)
- 10: $P_{n+1}(\mathbf{r}_{SLM}) = P_{n+1}(\mathbf{r}_{SLM} - \mathbf{s}_n + \mathbf{s}_n)$
- 11: **end for**
- 12: **end for**
- 13: $O(\mathbf{r}_{sample}) = prop_{-d1}(O_N^{SLM}(\mathbf{r}_{SLM}))$

3. Experimental result

We build up a lensless coherent imaging system based on SLM for performance verification in real experiments. The laser generator (THORLABS S4FC520) generates a stable 520nm coherent light source, which is then transformed into parallel light by a collimator. To verify the proposed method, we select a low-cost SLM (\$1500) with unknown modulation curve. The size of liquid crystal unit of SLM (tSLM-III) is $12.5 \mu m$ and the number of pixel is 1024×768 . The distance between the sample and the sensor ranges from 7 to 13 cm. After propagating a certain distance, the image sensor captures the modulated diffraction image. The image contains 2448×2048 pixels, and the pixel size is $3.45 \mu m$. The hardware configuration for reconstruction is as follows: GPU of GeForce GTX Titan X, RAM of 32GB, and CPU of Intel Core i9-9820X. The number of iterations is set to 10, and the reconstruction takes about 3 minutes.

In our experiments, we found that the light source and the graininess of the phase modulation pattern significantly impact the quality of the algorithm's reconstruction. When the light source is not collimated, it will interfere with the phase of the object in CCD plane, resulting in regular

fringes in the phase image and affecting the final phase recovery quality. In this regard, we first measured the complex amplitude distribution of the light source with the same experimental parameters, and then put the sample into the optical path to eliminate the effect of the light source on phase recovery by phase filtering. As shown in Fig. 4(a), the difference between the angle of light incidence causes periodically varying tilted fringes in the phase image. These disturbances can couple with the complex amplitude of the object and affect the recovery quality. The decoupled phase image is shown on the right side of Fig. 4(a), which significantly eliminates interference from laser sources. Furthermore, The modulation pattern has a significant impact on the quality of the reconstruction. The design of the pattern has been reported to influence the

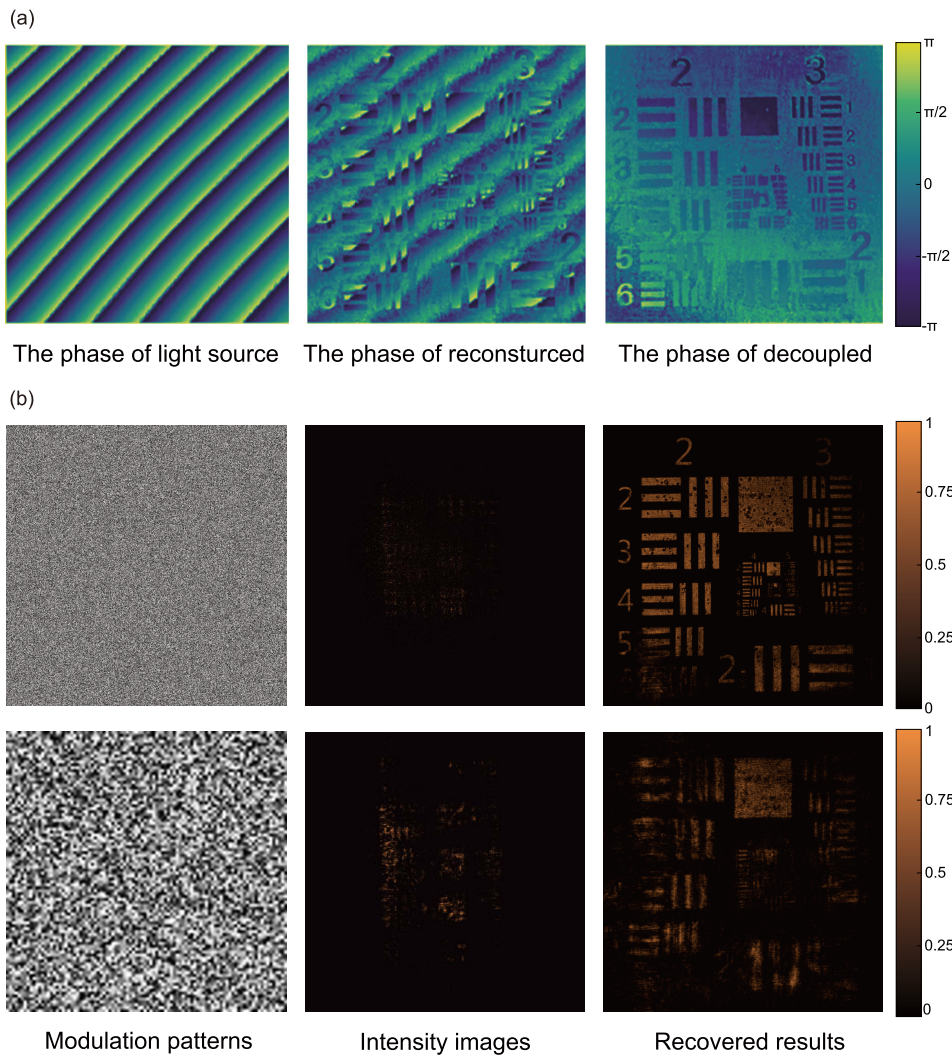


Fig. 4. (a) Phase reconstruction results of light source only, object mixing with light source, and decoupled object. (b) The left panel displays different modulation patterns, with the upper pattern exhibiting higher graininess compared to the lower one. The middle and right panels show the intensity images corresponding to these patterns and the resulting reconstructions, demonstrating that higher graininess in the modulation pattern enhances reconstruction quality.

reconstruction of complex amplitude [47]. To investigate this, we conducted an experiment to analyze the relationship between pattern modes and reconstruction quality. Since the resolution of SLM is $12.5 \mu\text{m}$, which is much larger than the $3.45 \mu\text{m}$ of the sensor, the graininess of the phase modulation pattern can greatly affect the reconstruction results, as shown in Fig. 4(b). The bottom modulation function in Fig. 4(b) is obtained by upsampling a random noise image of size 96×96 , and the upper one is satisfied with independent random distribution condition. It can be seen that the pattern with high randomness will have better reconstruction results. We also discussed the impact of the number of iterations and the number of intensity images used on the reconstruction results, with details provided in Fig.S3 of [Supplement 1](#).

In subsequent experiments, we implemented the described methods to reduce the influence of the light source and the graininess of the phase modulation pattern. To demonstrate the optimal reconstruction performance of our method, we calibrated the low-cost SLM modulation curve through a split-beam interference experiment, detailed in the [Supplement 1](#), and obtained an approximate true phase modulation curve. To quantify the performance of our method, we used a USAF phase target to evaluate the reconstruction effectiveness of the model. In Fig. 5(a), it is

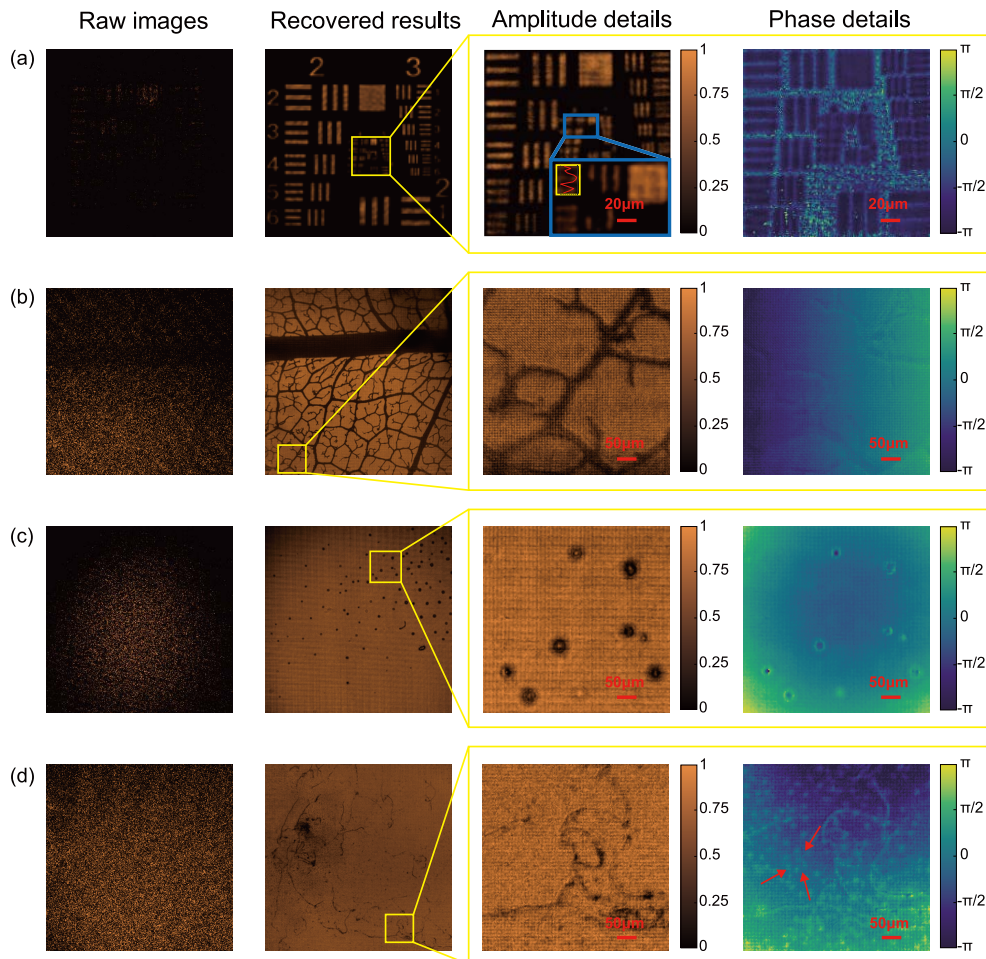


Fig. 5. The reconstructed results of the complex amplitude of (a) USAF-1951 resolution target, (b) leaf specimen, (c) stained cell slide, and (d) unstained cell slide.

able to resolve (6,2) sets of the USAF target with resolution of $14 \mu\text{m}$. Here (6,2) denotes the 6th group and the 2nd element in USAF, respectively, and the object is about 9 cm away from the sensor. The process of back propagation is also available in the [Visualization 2](#). Subsequently, we reconstructed the complex amplitude of both the leaf and the cells. in Fig. 5(b), We can clearly distinguish the veins of the leaf. Fig. 5(c) and (d) show the results of the reconstruction with and without staining the cells, respectively. In the amplitude image of Fig. 5(c), the shape of the cell can be distinguished, and the dark region is the stained cytoplasm. While in the phase image, the nucleus is distinct for its higher refractive index. Further, we evaluated the recovery quality of unstained biological sample. As shown in Fig. 5(d), the distribution of unstained cell is not visible in the amplitude image, but it can be clearly observed in the phase image (seeing red arrows in phase details). This reflects the characteristics of phase imaging, which enables imaging of samples with high transparency.

Moreover, our method can be applied to any unknown modulation curve of the SLM. We used the phase modulation values obtained from the linear SLM modulation curve and the calibration modulation curve as the input for the algorithm, as shown in Fig. 6. We performed comparative experiments on the stained cell slides. For the stained cell slides, 50 raw images were used for reconstruction with the ideal modulation curve, while 40 raw images were used with the calibration curve. The recovered results demonstrate that even without correcting the phase modulation values of the SLM, our method can still reconstruct comparable results. The successful reconstruction of the sample's complex amplitude using an ideal linear modulation curve as the algorithm input indicates that our method is capable of accurately recovering the complex amplitude, even when employing different SLMs with unknown modulation characteristics, provided that a default linear modulation curve is assumed.

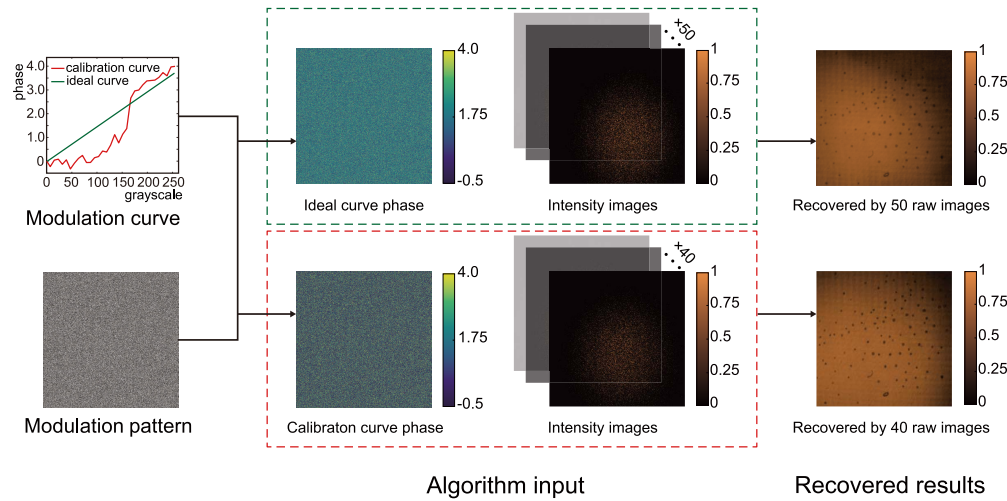


Fig. 6. The recovered results with unknown modulation curve on the stained cell slides.

Using the phase modulation values corresponding to the ideal modulation curve and the calibration modulation curve as inputs to the algorithm, comparable reconstruction quality can be achieved by utilizing a larger number of raw images.

4. Conclusion

In this paper, we report a low aberration and wide FOV lensless imaging system based on SLM. First, we build a forward diffraction model of the object in a coherent diffraction scenario. Due to errors in the modulation curve of the SLM, the complex amplitude information of the object

cannot be reconstructed using the APR or ePIE algorithms. Phase modulation errors in the SLM can cause deviations from the intended modulation values. As these errors accumulate, the high-frequency components of the diffraction pattern become attenuated, limiting the system's ability to extract high-resolution information effectively. Moreover, the presence of non-uniform phase errors induces spatially inconsistent shifts in the frequency domain, making it challenging for phase retrieval algorithms, such as APR or ePIE algorithm, to accurately reconstruct the original target information. Consequently, these errors degrade the accuracy of the recovered complex amplitude distribution. Therefore, we introduced the concept of ptychographic scanning with a spiral scan path, which, in combination with the ePIE algorithm, effectively restores the complex amplitude information of the object. Second, we eliminated the impact of the light source and the graininess of the phase modulation pattern on the reconstruction quality. Finally, we carry out a series of comparative experiments to evaluate the performance of our system. The reconstructed results show our lensless system can achieve to 14 μm resolution and is able to reduce the requirement of the accuracy of SLM. We believe this system can be further applied in other tasks such as tomography and microscopy in the future.

Funding. National Natural Science Foundation of China (Grant 62031023, Grant 62331011); Shenzhen Science and Technology Project (Grant GXWD20220818170353009).

Disclosures. The authors declare no conflicts of interest.

Data availability. Data underlying the results presented in this paper are not publicly available at this time but may be obtained from the authors upon reasonable request.

Supplemental document. See [Supplement 1](#) for supporting content.

References

1. J. Zhang, Q. Chen, J. Li, *et al.*, "Lensfree dynamic super-resolved phase imaging based on active micro-scanning," *Opt. Lett.* **43**(15), 3714–3717 (2018).
2. A. Ozcan and U. Demirci, "Ultra wide-field lens-free monitoring of cells on-chip," *Lab Chip* **8**(1), 98–106 (2008).
3. J. Zhang, J. Sun, Q. Chen, *et al.*, "Adaptive pixel-super-resolved lensfree in-line digital holography for wide-field on-chip microscopy," *Sci. Rep.* **7**(1), 11777 (2017).
4. A. Coskun, T. Su, and A. Ozcan, "Wide field-of-view lens-free fluorescent imaging on a chip," *Lab Chip* **10**(7), 824 (2010).
5. J. Zhang, J. Sun, Q. Chen, *et al.*, "Resolution analysis in a lens-free on-chip digital holographic microscope," *IEEE Trans. Comput. Imaging* **6**, 697–710 (2020).
6. A. Ozcan and E. McLeod, "Lensless imaging and sensing," *Annu. Rev. Biomed. Eng.* **18**(1), 77–102 (2016).
7. C. Guo, F. Zhang, X. Zhang, *et al.*, "Lensfree super-resolved imaging based on adaptive wiener filter and guided phase retrieval algorithm," *J. Opt.* **22**(5), 055703 (2020).
8. R. Egami, R. Horisaki, L. Tian, *et al.*, "Relaxation of mask design for single-shot phase imaging with a coded aperture," *Appl. Opt.* **55**(8), 1830–1837 (2016).
9. J. K. Adams, V. Boominathan, B. W. Avants, *et al.*, "Single-frame 3d fluorescence microscopy with ultraminiature lensless flatscope," *Sci. Adv.* **3**(12), e1701548 (2017).
10. T. Shimano, Y. Nakamura, K. Tajima, *et al.*, "Lensless light-field imaging with fresnel zone aperture: quasi-coherent coding," *Appl. Opt.* **57**(11), 2841–2850 (2018).
11. V. Boominathan, J. K. Adams, J. T. Robinson, *et al.*, "Phlatcam: Designed phase-mask based thin lensless camera," *IEEE Trans. Pattern Anal. Mach. Intell.* **42**(7), 1618–1629 (2020).
12. X. Pan, X. Chen, S. Takeyama, *et al.*, "Image reconstruction with transformer for mask-based lensless imaging," *Opt. Lett.* **47**(7), 1843–1846 (2022).
13. J. Chen, F. Wang, Y. Li, *et al.*, "Lensless computationally defined confocal incoherent imaging with a fresnel zone plane as coded aperture," *Opt. Lett.* **48**(17), 4520–4523 (2023).
14. S. S. Khan, V. Sundar, V. Boominathan, *et al.*, "Flatnet: Towards photorealistic scene reconstruction from lensless measurements," *IEEE Trans. Pattern Anal. Mach. Intell.* **44**(4), 1934–1948 (2020).
15. H. Zhou, H. Feng, W. Xu, *et al.*, "Deep denoiser prior based deep analytic network for lensless image restoration," *Opt. Express* **29**(17), 27237–27253 (2021).
16. K. Yanny, K. Monakhova, R. W. Shuai, *et al.*, "Deep learning for fast spatially varying deconvolution," *Optica* **9**(1), 96–99 (2022).
17. Y. Li, Z. Li, K. Chen, *et al.*, "Mwdns: reconstruction in multi-scale feature spaces for lensless imaging," *Opt. Express* **31**(23), 39088–39101 (2023).
18. X. Cai, Z. You, H. Zhang, *et al.*, "Phocolens: Photorealistic and consistent reconstruction in lensless imaging," *arXiv* (2024).

19. D. J. Brady, K. Choi, D. L. Marks, *et al.*, "Compressive holography," *Opt. Express* **17**(15), 13040–13049 (2009).
20. Y. Rivenson, Y. Zhang, H. Günaydin, *et al.*, "Phase recovery and holographic image reconstruction using deep learning in neural networks," *Light: Sci. Appl.* **7**(2), 17141 (2018).
21. Y. Wu, Y. Luo, G. Chaudhari, *et al.*, "Bright-field holography: cross-modality deep learning enables snapshot 3D imaging with bright-field contrast using a single hologram," *Light: Sci. Appl.* **8**(1), 25 (2019).
22. L. Waller, L. Tian, and G. Barbastathis, "Transport of intensity phase-amplitude imaging with higher order intensity derivatives," *Opt. Express* **18**(12), 12552–12561 (2010).
23. L. Waller, S. S. Kou, C. J. R. Sheppard, *et al.*, "Phase from chromatic aberrations," *Opt. Express* **18**(22), 22817–22825 (2010).
24. M. K. Kim, L. Yu, and C. J. Mann, "Interference techniques in digital holography," *J. Opt. A: Pure Appl. Opt.* **8**(7), S518–S523 (2006).
25. C. Oh, S. O. Isikman, B. Khademhosseini, *et al.*, "On-chip differential interference contrast microscopy using lensless digital holography," *Opt. Express* **18**(5), 4717–4726 (2010).
26. P. Vora, V. Trivedi, S. Mahajan, *et al.*, "Wide field of view common-path lateral-shearing digital holographic interference microscope," *J. Biomed. Opt.* **22**, 1–11 (2017).
27. Y. Gao and L. Cao, "Motion-resolved, reference-free holographic imaging via spatiotemporally regularized inversion," *Optica* **11**(1), 32–41 (2024).
28. J. Miao, R. L. Sandberg, and C. Song, "Coherent x-ray diffraction imaging," *IEEE J. Sel. Top. Quantum Electron.* **18**(1), 399–410 (2012).
29. K. A. Nugent, "Coherent methods in the x-ray sciences," *Adv. Phys.* **59**(1), 1–99 (2010).
30. R. Horisaki, R. Takagi, and J. Tanida, "Learning-based imaging through scattering media," *Opt. Express* **24**(13), 13738–13743 (2016).
31. J. M. Rodenburg and H. M. L. Faulkner, "A phase retrieval algorithm for shifting illumination," *Appl. Phys. Lett.* **85**(20), 4795–4797 (2004).
32. S. Jiang, J. Zhu, P. Song, *et al.*, "Wide-field, high-resolution lensless on-chip microscopy via near-field blind ptychographic modulation," *Lab Chip* **20**(6), 1058–1065 (2020).
33. C. Lu, Y. Zhou, Y. Guo, *et al.*, "Mask-modulated lensless imaging via translated structured illumination," *Opt. Express* **29**(8), 12491–12501 (2021).
34. B. Wang, Z. He, and F. Zhang, "Coherent modulation imaging using unknown modulators," *Opt. Express* **29**(19), 30035–30044 (2021).
35. S. Jiang, C. Guo, P. Song, *et al.*, "Resolution-enhanced parallel coded ptychography for high-throughput optical imaging," *ACS Photonics* **8**(11), 3261–3271 (2021).
36. S. Jiang, P. Song, T. Wang, *et al.*, "Spatial-and fourier-domain ptychography for high-throughput bio-imaging," *Nat. Protoc.* **18**(7), 2051–2083 (2023).
37. L. Liu, W. Li, M. Gong, *et al.*, "Resolution-enhanced lensless ptychographic microscope based on maximum-likelihood high-dynamic-range image fusion," *IEEE Trans. Instrum. Meas.* **73**(4502711), 4502711 (2024).
38. G. Weinberg, M. Kang, W. Choi, *et al.*, "Ptychographic lensless coherent endomicroscopy through a flexible fiber bundle," *Opt. Express* **32**(12), 20421–20431 (2024).
39. P. Song, R. Wang, L. Loetgering, *et al.*, "Ptycho-endoscopy on a lensless ultrathin fiber bundle tip," *Light: Sci. Appl.* **13**(1), 168 (2024).
40. M. DeWeert and B. Farm, "Lensless coded-aperture imaging with separable doubly-toeplitz masks," *Opt. Eng.* **54**(2), 023102 (2015).
41. Y. Wu, M. K. Sharma, and A. Veeraraghavan, "Wish: wavefront imaging sensor with high resolution," *Light: Sci. Appl.* **8**(1), 44 (2019).
42. Z. Liu, C. Guo, J. Tan, *et al.*, "Iterative phase-amplitude retrieval with multiple intensity images at output plane of gyrator transforms," *J. Opt.* **17**(2), 025701 (2015).
43. A. M. Maiden and J. M. Rodenburg, "An improved ptychographical phase retrieval algorithm for diffractive imaging," *Ultramicroscopy* **109**(10), 1256–1262 (2009).
44. T. Wang, S. Jiang, P. Song, *et al.*, "Optical ptychography for biomedical imaging: recent progress and future directions," *Biomed. Opt. Express* **14**(2), 489–532 (2023).
45. Y. Zhou, B. Xiong, X. Li, *et al.*, "Lensless imaging of plant samples using the cross-polarized light," *Opt. Express* **28**(21), 31611–31623 (2020).
46. X. Huang, H. Yan, R. Harder, *et al.*, "Optimization of overlap uniformness for ptychography," *Opt. Express* **22**(10), 12634–12644 (2014).
47. O. Cossairt, M. Gupta, and S. K. Nayar, "When does computational imaging improve performance?" *IEEE Trans. on Image Process.* **22**(2), 447–458 (2013).